Solar Energy 258 (2023) 325–338

Contents lists available at ScienceDirect

Solar Energy

journal homepage: www.elsevier.com/locate/solener

$NaNO_3$-KNO_3/EG/Al_2O_3 shape-stable phase change materials for thermal energy storage over a wide temperature range: Sintering temperature study

Mengting Ji, Laiquan Lv, Jingwen Liu, Yan Rong, Hao Zhou *

State Key Laboratory of Clean Energy Utilization, Institute for Thermal Power Engineering, Zhejiang University, Hangzhou 310027, PR China

ARTICLE INFO

Keywords:
Shape-stable phase change materials
Wide temperature range
Sintering temperature
Thermal energy storage
Binary nitrate

ABSTRACT

The coefficient of thermal expansion of inorganic salts increases with increasing temperature. The sintering temperature may affect the properties of the shape-stable phase change materials (SSPCMs). We study the SSPCMs with $NaNO_3$-KNO_3 as the phase change material and Al_2O_3 and expanded graphite (EG) as the skeletal support materials (SSMs) to achieve thermal energy storage over a wide temperature range. The effects of different sintering temperatures on the SSMs content, thermal conductivity and compressive strength of SSPCMs were studied. The results showed that as the sintering temperature increased, more SSMs were required to support the SSPCMs. The maximum $NaNO_3$-KNO_3 mass percentages of the SSPCMs sintered at 300 °C and 450 °C were 82.8 wt% and 66.4 wt%, respectively. Samples with application temperatures higher than the sintering temperature may have problems stabilizing the shape. Sintering temperature had little influence on the thermal conductivity of the same SSPCMs. However, the compressive strength of the SSPCMs decreased with increasing sintering temperature. The addition of EG decreases the decomposition temperature of the composite and limits its application temperature range. The SSPCM-10/30 sintered at 450 ℃ showed good chemical stability performance, and the latent heat decreased from 56.01 J/g to 53.44 J/g. The compressive strength dropped from 30.7 MPa to 25.17 MPa before and after 20 cycles due to larger internal gaps and did not change much after 20 cycles.

1. Introduction

Many countries have recently committed to becoming carbon neutral [32,10]. With global energy consumption increasing yearly, deeper renewable energy penetration and more efficient energy technologies are among the essential measures to decarbonize energy systems [9]. The intermittent and volatile nature of renewable energy is a key barrier to the deployment of this technology on a large scale. Practical thermal energy storage (TES) can decrease the energy supply–demand mismatch and increase the efficiency of energy systems [54]. There are three main categories of TES technologies, depending on the storage medium: sensible thermal storage, latent thermal storage (LHS) and thermochemical thermal storage. Among them, LHS based on phase change materials (PCM) has received great attention recently due to its advantages such as stable storage temperature, favorable reasonable energy storage density and investment in capital [25]. In terms of medium to high temperature (>100 °C) TES [20], PCM can be applied in solar power systems, industrial waste heat recovery, peak load transfer, cogeneration, etc.

Inorganic salts have a suitable melting point and latent heat, and have a good future in medium and high-temperature TES applications [25]. Inorganic salts can be classified as nitrate, carbonate, fluoride and chloride salts. Binary and ternary eutectic salts extend the working temperature range [22]. Among the commonly used molten salt mixtures are Solar Salt (60$NaNO_3$-40KNO_3), HitecXL (7$NaNO_3$-45KNO_3-48$Ca(NO_3)_2$, HITEC (7$NaNO_3$-53KNO_3-40$NaNO_2$) etc., and their thermophysical properties are shown in the literature [13]. Herein, the values in front of the compounds represent weight fractions.

Shape-stable phase change materials (SSPCMs) have recently been developed to overcome the problems of liquid phase leakage, low thermal conductivity and corrosion of inorganic salts. Such SSPCMs are typically made of PCMs, skeletal support materials (SSMs) for stabilizing the shape, and thermal conduction enhancement additives (TCEAs) [25,20]. SSMs can be classified as polymeric, metallic, ceramic and carbon. The maximum application temperature of 400 °C for polymeric matric is not suitable for the thermal storage of inorganic salts over a large temperature range. The corrosion of metallic matric by inorganic salts is also a problem. Ceramic matric and carbon matric have better prospects for application as SSMs for inorganic salts. Ceramic matric can

* Corresponding author.
E-mail address: zhouhao@zju.edu.cn (H. Zhou).

https://doi.org/10.1016/j.solener.2023.04.048
Received 18 January 2023; Received in revised form 2 April 2023; Accepted 22 April 2023
Available online 13 May 2023

Nomenclature

Abbreviation

CCHS	Cold compression and hot sintering
EG	Expanded graphite
LHS	Latent thermal storage
PCM	Phase change material
SEM	Scanning Electron Microscope
SSM	Skeletal support material
SSPCM	Shape-stable phase change material
TCEA	Thermal conduction enhancement additive
TCI	Thermal conductivity instrument
TES	Thermal energy storage
TG	Thermogravimetric
XRD	X-ray diffractometer

Greek symbols

m_{EG}	Weight of EG, g
$m_{(EG+salt)}$	Weight of EG and salt, g
m_1	Weight of the samples before thermal cycling, g
m_2	Weight of the samples after thermal cycling, g
T_m	Melting point, ℃
T_s	Sintering temperature, ℃
ΔH_{PCM}	Latent heat of $NaNO_3$-KNO_3, J/g
ΔH_{theory}	Theoretical latent heat of SSPCM, J/g
ΔT_{s-m}	Difference between T_s and T_m, ℃
η	EG mass fraction, %
θ	Al_2O_3 mass fraction, %
λ	Thermal conductivity, W/(m·K)

Table 1
Investigation of inorganic salt-based SSPCMs by the CCHS method.

Composite	Matrix	Matrix ratio (wt%)	T_m (°C)	T_s (°C)	ΔT_{s-m} (°C)	Cp (kJ/kg·℃)	K (W/m·K)	ΔH (kJ/kg)	Refs.
$Ca(NO_3)_2$-$NaNO_3$	EG	7	217	300	83.2	1.2539	5.7	89.79	[39]
$MgCl_2$-KCl	EG	15	424	500	75.86	–	4.922	161.37	[33]
$Ca(NO_3)_2$-KNO_3-$NaNO_3$-$NaNO_2$	MgO: graphite	50:10	90	250	160.4	–	1.403	37.71	[27]
$MgCl_2$-KCl-$CaCl_2$	MgO: EG	40:15	386	500	113.7	–	8.86	81.1	[12]
K_2CO_3-Li_2CO_3-Na_2CO_3	MgO	50	386	600	213.6	1.48 (450–600 °C)	–	158.7	[40]
Li_2CO_3-Na_2CO_3	MgO: graphite	50:10	498	550	51.7	–	4.3	178.3	[8]
$LiNO_3$-$NaNO_3$-KNO_3-$Ca(NO_3)_2$	calcium silicate	20	104	150	46.5	1.65 (123–200 °C)	1.177	73.59	[19]
$NaNO_3$	SiO_2: graphite	30:10	304	350	46.4	–	–	79.35	[34]
$NaNO_3$	diatomite: graphite	30:10	308	370	62.2	1.65 (20–250 °C)	3	115.79	[49]
KNO_3	diatomite	35	330	350	19.77	–	–	60.52	[6]
Na_2CO_3-K_2CO_3	MgO: SiC	40:10	710	750	40	1.65	2.28	110.2	[18]
Na_2CO_3	MgO: MWCNT	40:0.5	851	900	49	–	1.489	–	[52]
Na_2SO_4-NaCl	mullite	55	626	680	54	–	1.95 (100 °C)	117.6	[16]
NaCl-KCl	diatomite	30	657	680	23	1.07 (550–750 °C)	–	179.3	[23]

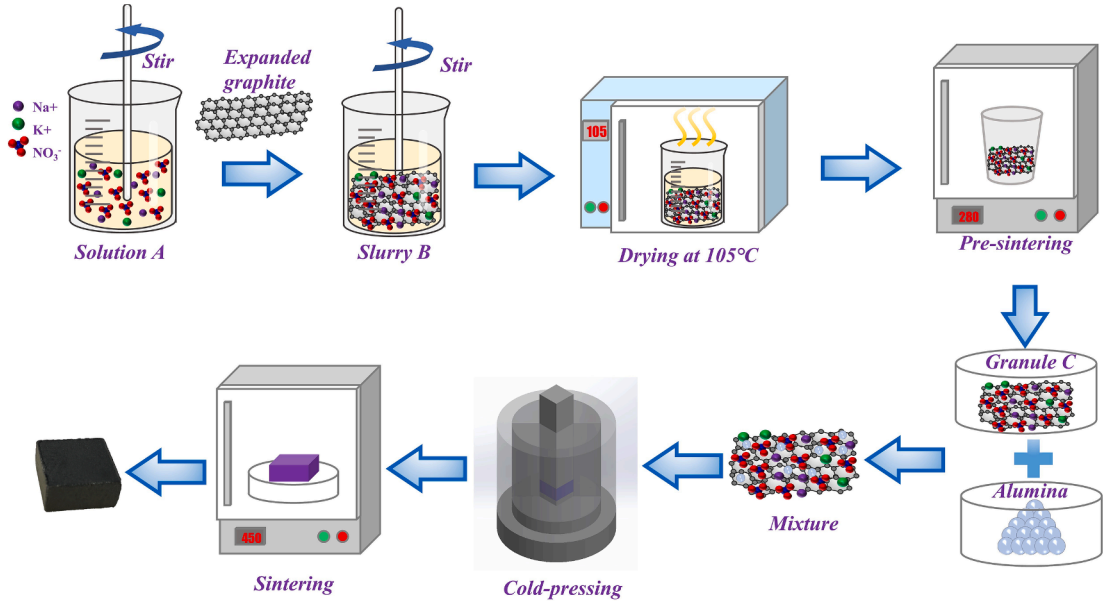

Fig. 1. Schematic diagram of SSPCMs fabrication method.

be divided into porous and non-porous matric according to their structural characteristics [20]. Porous ceramics rely on capillary forces to retain molten PCM due to their porous structure and the voids between the particles [14]. e.g. diatomite [37,36,49,6], vermiculite [48,28] and expanded perlite [42,29]. Non-porous ceramics rely on interstitial spaces between particles to retain molten PCM. e.g. MgO [27,8,40], SiO_2 [11,46], Al_2O_3 [43,16,17] and kaolin [55].

Carbon media can be used both as porous materials to stabilize the

Table 2
Mass ratio of materials for SSPCMs.

Sample	$m_{EG}/m_{(EG+salt)}$	Al_2O_3 (wt %)	EG (wt %)	$NaNO_3$-KNO_3 (wt %)
SSPCM-5EG	5	0	5	95
SSPCM-8EG	8	0	8	92
SSPCM-10EG	10	0	10	90
SSPCM-5/10	5	10	4.5	85.5
SSPCM-8/10	8	10	7.2	82.8
SSPCM-10/10	10	10	9	81
SSPCM-5/20	5	20	4	76
SSPCM-8/20	8	20	6.4	73.6
SSPCM-10/20	10	20	8	72
SSPCM-5/30	5	30	3.5	66.5
SSPCM-8/30	8	30	5.6	64.4
SSPCM-10/30	10	30	7	63

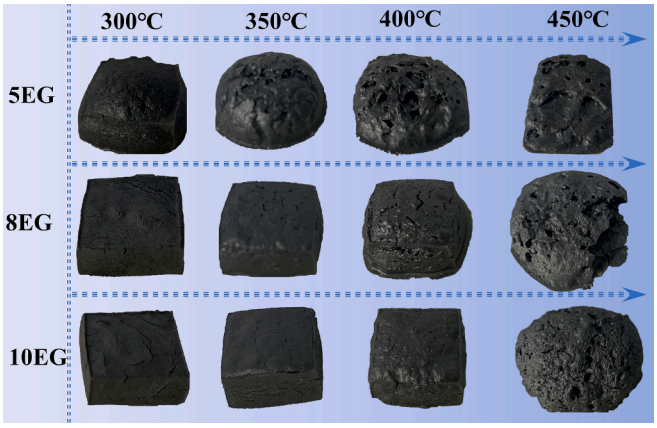

Fig. 2. The photographs of the SSPCM-5EG, SSPCM-8EG and SSPCM-10EG sintered at different temperatures.

inorganic salt composites in shape and as TCEAs to improve the thermal conductivity of SSPCMs. Ren et al. [39] fabricated $Ca(NO_3)_2$-$NaNO_3$/ EG composites and the results showed that the 7 wt% EG composite had good properties. Sang et al. [41] prepared KCl-LiCl/EG SSPCMs with various EG contents, and 80KCl-LiCl/20EG was the most desirable SSPCM ratio. Liu et al. [33] prepared $MgCl_2$-KCl/EG composites, and the largest salt mass loading was 85%. Li et al. [27] prepared $Ca(NO_3)_2$-KNO_3-$NaNO_3$-$NaNO_2$/MgO/graphite composites where graphite was as TCEA. Hou et al. [12] fabricated $MgCl_2$-KCl-$CaCl_2$/MgO/EG composites and the composites with 40 wt% MgO and 15 wt% EG performed best. By comparison, we found that the inorganic salt/EG composites prepared by the solution impregnation method by Ren et al. [39] can achieve better performance at a smaller EG mass percentage.

The fabrication methods of SSPCMs are classified into cold compression and hot sintering (CCHS), infiltration impregnation and Sol-gel [20,15]. The CCHS methods have received much attention due to their suitability for industrial mass production [25,12]. Cold compression is used to make a tight connection between PCM and SSM, and sintering the composites at temperatures above the melting temperature of PCM is used to make the liquid PCM wet and diffuse onto the solid grains of SSM, creating interfacial forces between the molten salt and the ceramics. The interfacial forces can hold these ceramic grains together, leading to the rearrangement and densification of these composites [17]. Table 1 summarizes the recent years of research on inorganic salt-based SSPCMs. Salt-based composites are made at fixed sintering temperatures, and the sintering temperatures (T_s) are mostly concentrated near the melting point (T_m) of PCMs ($\Delta T_{s\text{-}m} = T_s\text{-}T_m < 100$ °C). When $\Delta T_{s\text{-}m}$ is large, more SSMs are often required to maintain the shape stability of

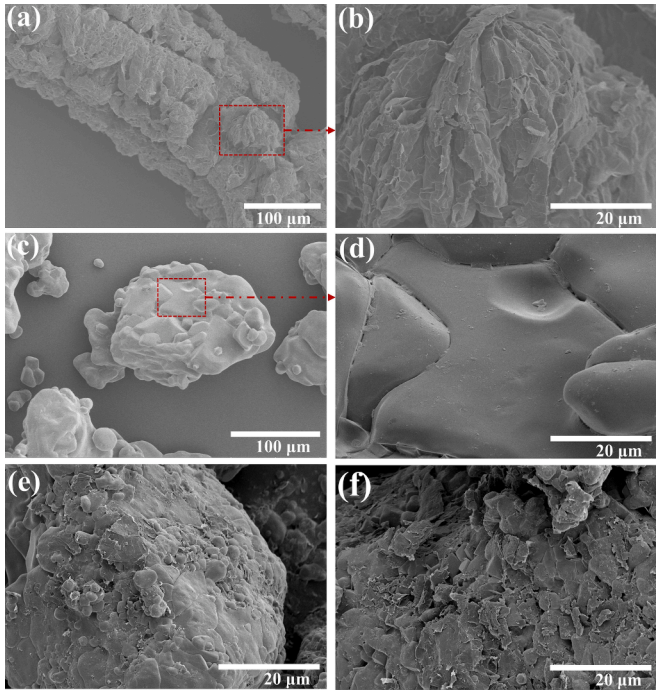

Fig. 3. SEM photos of pure EG particles (a) ×350, (b) ×2000, $NaNO_3$-KNO_3 (c) ×350, (d) ×2000, (e) SSPCM-5EG and (f) SSPCM-10EG.

the composite. For example, $\Delta T_{s\text{-}m}$ in the literature [27,12,19] were 160.4, 113.7 and 213.6 °C, and inorganic salts were 45 wt%, 50 wt% and 50 wt%, respectively. Inorganic salts have the advantage of a wide range of thermal storage temperature range, such as Solar Salts have been widely used as sensible thermal fluid in the temperature range of 290-560 °C. Most application temperature ranges of composite PCMs rely on the thermogravimetric (TG) method to analyze the decomposition temperature of the material to obtain the maximum application temperature [19]. However, this only ensures that the composite does not decompose below the decomposition temperature and cannot guarantee shape stability. The coefficient of thermal expansion of inorganic salts increases with the temperature. For example, Solar Salt density as a function of temperature can be expressed as $\rho[kg/m^3] = 2091 - 0.641 \times T(°C)$ from 260 °C to 593 °C [4]. This means that the volume per unit mass of Solar Salt may increase by 12% from 260 °C to 593 °C. Different sintering temperatures may affect the properties of SSPCMs. At a lower sintering temperature, the molten liquid collects particles of the skeletal material under capillary forces and bonds them after salt solidification. As a result, the composite can form a dense microstructure after sintering, and the PCM can be embedded in the skeletal materials' pores or gaps. However, if the application temperature is much higher than the sintering temperature, the interior of the composite may not be able to accommodate the volume expansion of the PCM. The SSPCM morphology and performance may change. Ren et al. [38] investigated the effect of the preparation process (including stirring rate, evaporation temperature, impregnation temperature, cold pressing pressure, and sintering temperature) on Ca$(NO_3)_2$-KNO_3/EG. They only studied the effect of sintering temperature on morphology, and the maximum studied value of $\Delta T_{s\text{-}m}$ was about 120 °C. It was confirmed that 300 °C makes the optimum operating temperature, and the composites' properties in a wide temperature range were not described in detail. Studying the effect of sintering temperature on the properties of SSPCMs makes the SSPCMs positive for wide temperature range applications.

The mechanical properties of SSPCMs are an important guarantee for the effective long-term operation of the TES system. The compressive strength directly affects the mechanical properties of SSPCMs [40]. The

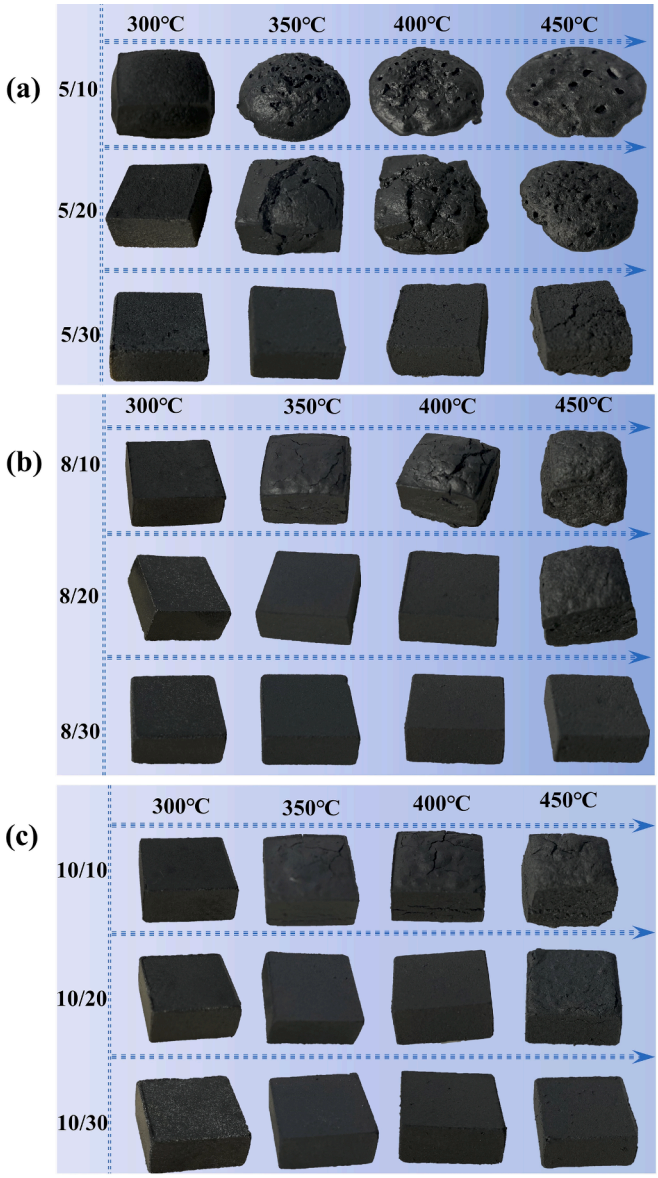

Fig. 4. The photographs of the SSPCMs sintered at different temperatures.

Table 3
Degree of deformation of SSPCMs at different sintering temperatures.

T_s (°C)	SSPCM-								
	5/10	5/20	5/30	8/10	8/20	8/30	10/10	10/20	10/30
300	×	☆	☆	☆	☆	☆	☆	☆	☆
350	×	×	☆	○	☆	☆	○	☆	☆
400	×	×	☆	×	☆	☆	×	☆	☆
450	×	×	×	×	○	☆	×	○	☆

(a) × represents SSPCMs with severe deformation and leakage;
(b) ○ represents the SSPCMs with a little shape deformation and leakage;
(c) ☆ represents the SSPCMs with structural integrity, no deformation and leakage.

addition of the appropriate amount of ceramic matrix can exhibit better compression resistance than EG-based SSPCMs [41]. Jiang et al. [17] found that 68.05 Na_2SO_4-31.95 NaCl/α-Al_2O_3 exhibited better cycling performance. However, α-Al_2O_3 requires high-temperature calcination, and in contrast, γ-Al_2O_3 is synthesized at a lower temperature and thus consumes less energy [5]. In this study, we investigated the composite

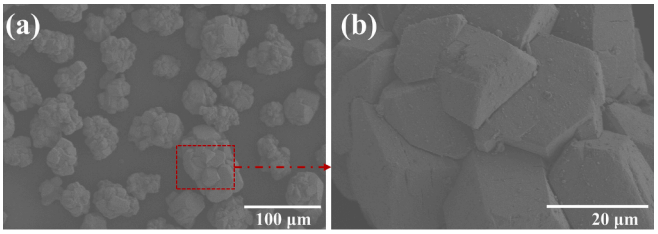

Fig. 5. SEM photos of (a-b) pure Al_2O_3 particles with the magnification of 300x, 2000x.

materials with $NaNO_3$-KNO_3 as PCM, γ-Al_2O_3 as SSM, EG as SSM and TCEA. The fabrication of $NaNO_3$-KNO_3/EG composites by solution impregnation method was used to achieve the adsorption of EG on PCM. Then the $NaNO_3$-KNO_3/γ-Al_2O_3/EG composite phase change materials were fabricated by the CCHS method. SSPCMs were investigated for their chemical stability, macro- and micro-morphology, thermal conductivity, mechanical properties, thermal properties, and cyclic stability performance at different sintering temperatures (300, 350, 400, 450, and 500 °C).

2. Materials and methods

2.1. Raw materials

In this work, PCM consisted of 60 wt% $NaNO_3$ and 40 wt% KNO_3. Zhejiang Lianda Chemical Co. Ltd. supplied it with more than 99.5% purity. Expandable graphite flakes were purchased from China Aladdin Chemical Co. Ltd. with a diameter of about 75 μm. In this paper, expanded graphite flakes were placed in an 800 W microwave oven for 30 s to obtain EG. Activated Al_2O_3 (AR, Sinopharm Chemical Reagent Co., Ltd.) was selected as the ceramic SSM. Deionized water was obtained in the laboratory.

2.2. The manufacturing procedure of SSPCMs

The SSPCMs were fabricated in two steps, and Fig. 1 shows the fabrication process of SSPCMs. The fabrication of SSPCMs was performed in two steps. The first step was the preparation of the $NaNO_3$-KNO_3/EG mixture powder, including EG impregnation into $NaNO_3$-KNO_3 solution, pre-sintering and crushing. In detail, 200 g of $NaNO_3$-KNO_3 was weighed and poured into a beaker containing 300 ml of deionized water. The beaker was placed into a heat-collecting magnetic stirrer with the water bath temperature set at 68 °C, and the solution was stirred continuously to completely dissolve $NaNO_3$-KNO_3 in water to form Solution A. A specific mass of EG was weighed (i.e., EG: $NaNO_3$-KNO_3 = 5:95, 8:92 and 10:90), and EG was slowly added to Solution A, stirring continuously for 15 min to form a $NaNO_3$-KNO_3 /EG slurry (Slurry B). Then Slurry B was placed in an oven at 105 °C for 24 h to make the water in Slurry B evaporate completely. The $NaNO_3$-KNO_3/EG mixture was pre-sintered in a muffle furnace at 280 °C for 5 h to allow $NaNO_3$-KNO_3 to be more fully adsorbed by EG. Finally, the $NaNO_3$-KNO_3/EG mixture was removed from the muffle furnace and the $NaNO_3$-KNO_3/EG were crushed into powders (Granule C) using a planetary miller at 1800 rpm for 1 min.

The second step is mixing, cold pressing and sintering. The $NaNO_3$-KNO_3/EG mixture powder and Al_2O_3 powder were weighed in a certain mass ratio and mixed well with a mortar. The name of the samples and the mass fraction of each component are shown in Table 2. The samples in Table 2 are named SSPCM-xxEG or SSPCM-xx/yy, where xx represents the mass fraction of EG in the $NaNO_3$-KNO_3/EG mixture in the first step, i.e., $m_{EG}/m_{(EG+salt)}$ is the value of xx. yy represents the mass fraction of Al_2O_3 in the SSPCM, and Al_2O_3 (wt%) is the value of yy. EG (wt%) and $NaNO_3$-KNO_3 (wt%) represent the mass fraction of EG and $NaNO_3$-KNO_3 in the SSPCMs, respectively, where EG (wt%) = aa × (100-yy)/100 and

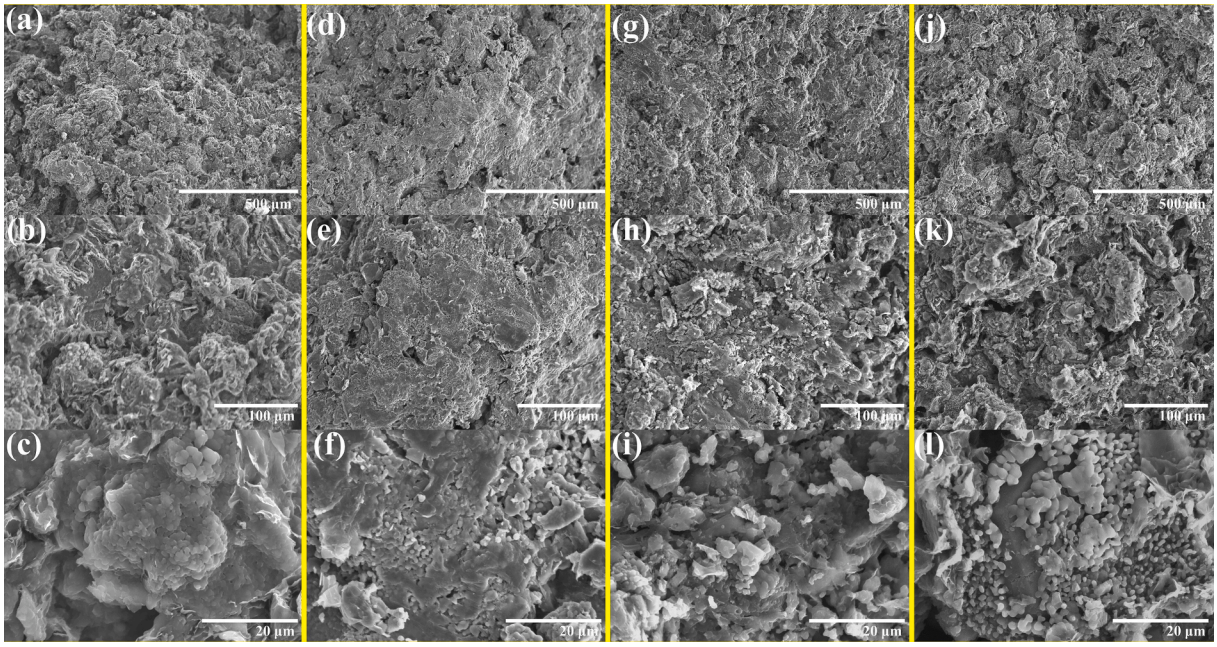

Fig. 6. SEM photos of (a-c) SSPCM-8/30, (d-f) SSPCM-10/10, (g-i) SSPCM-10/20, (j-l) SSPCM-10/30 sintered at 300 °C with the magnification of 100x, 350x, and 2000x.

$NaNO_3$-KNO_3 (wt%) = 100-yy- EG (wt%). About 3 g $NaNO_3$-KNO_3/EG/Al_2O_3 mixture powder was poured into a stainless steel mold and placed on a tableting machine. The sample was maintained at a pressure of 3.6 T for 60 s and compressed into a rectangular body with a cross-section of 15 mm × 15 mm and a thickness of about 6.8 mm. The compressed samples were placed into a muffle furnace and sintered by the following procedure: Heating at 5 °C/min from 30 °C to 105 °C, holding at 105 °C for 0.5 h to evaporate water, heating at 5 °C/min from 105 °C to 300, 350, 400, 450 and 500 °C, holding at the specified temperature for 2.5 h, and finally cooling at 5 °C/min. Each SSPCM was done more than 3 times during the investigation to ensure reproducible results.

2.3. Characterization

We observed the microstructures and element distributions of EG, Al_2O_3, $NaNO_3$-KNO_3, and SSPCMs using a field emission electron microscope (FESEM, SU8010, HITACHI, Japan) at a 3 kV acceleration voltage. X-ray diffractometer (XRD, X' pert Powder, Netherland) at 10° to 80° Cu K-α radiation (K = 1.540598 Å) was used to test the crystal sizes of EG, Al_2O_3, $NaNO_3$-KNO_3 and SSPCMs. The scanning rate is 0.1°/min and the step size is 0.02°. The thermal decomposition temperature was analyzed with a simultaneous thermal analyzer (STA 6000, PerkinElmer, USA) under a nitrogen atmosphere with a heating rate of 10 °C/min, and the temperature range was 50-800 °C.

The melting points and latent heats of $NaNO_3$-KNO_3 and SSPCMs were studied by a differential scanning calorimeter (TA, Q200, USA) with sample weights between 6 and 8 mg. The samples were heated from 100 to 300 °C at a rate of 10 °C/min and then cooled from 300 to 100 °C at a rate of 10 °C/min in a nitrogen atmosphere.

The electronic universal testing machine (CMT5205, Shenzhen New Sansi Metrology Technology Co., Ltd.) measured the SSPCM's mechanical strength. During the test, the tester's extrusion head operated at a speed of 1.0 mm/min. The maximum pressure corresponded to the point of a sudden drop. The mechanical strength corresponded to the maximum pressure strength [51].

The thermal conductivity of the binary nitrate and SSPCMs was measured by the C-Therm thermal conductivity instrument (TCI) at a room temperature of 27 ± 1 °C. The TCI sensor diameter is 17 mm, and the diameter of the measured sample needs to be larger than the sensor diameter. Therefore, cylindrical samples with Φ = 25 mm and about 6 mm thickness were prepared to study the thermal conductivity of SSPCM-5/30, SSPCM-8/30, and SSPCM-10/30 at different sintering temperatures.

2.4. Thermal cycling test

The thermal cycling test was operated in a muffle furnace. First, the SSPCMs-10/30 sintered at 450 °C were placed in a muffle furnace for 15 min at 450 °C to ensure complete melting of $NaNO_3$-KNO_3. Finally, the samples were cooled naturally at room temperature for 15 min to complete the solidification process. This cycle was repeated 100 times.

3. Results and discussion

3.1. Appearance and microstructure of prepared SSPCMs

3.1.1. Micro- and macro-morphology of $NaNO_3$-KNO_3/EG

Fig. 2 shows the macros images of SSPCM-5EG, SSPCM-8EG, and SSPCM-10EG sintered at different temperatures. Unfortunately, no material satisfied the feature of an intact shape structure. As the sintering temperature increased, the composites containing EG were more deformed, and the surface of the sintered samples was brighter, indicating the PCM's leakage. This may be because the coefficient of thermal expansion of binary nitrates increases with increasing temperature. The gaps between SSPCM of the same species were consistent at a specific compression pressure. The space reserved inside the SSPCM could not accommodate the volume expansion of $NaNO_3$-KNO_3, so $NaNO_3$-KNO_3 leakage occurred. With the increased EG content, the SSPCM deformed less at the same sintering temperature, which explained the EG adsorption capacity.

Fig. 3 shows the SEM photos of EG, $NaNO_3$-KNO_3, SSPCM-5EG and SSPCM-10EG. As shown in Fig. 3(a-b), the EG showed a loose and porous worm-like structure with many lamellar structures. As shown in Fig. 3(e-f), the lamellar structure of EG could not be clearly seen in the composite materials, which indicated that the $NaNO_3$-KNO_3 was well-filled into the EG lamellar structure. When the EG content was 5 wt%, the lamellar structure of EG did not adsorb the $NaNO_3$-KNO_3 well. The excess $NaNO_3$-KNO_3 adhered to the surface of EG and was more likely to aggregate into

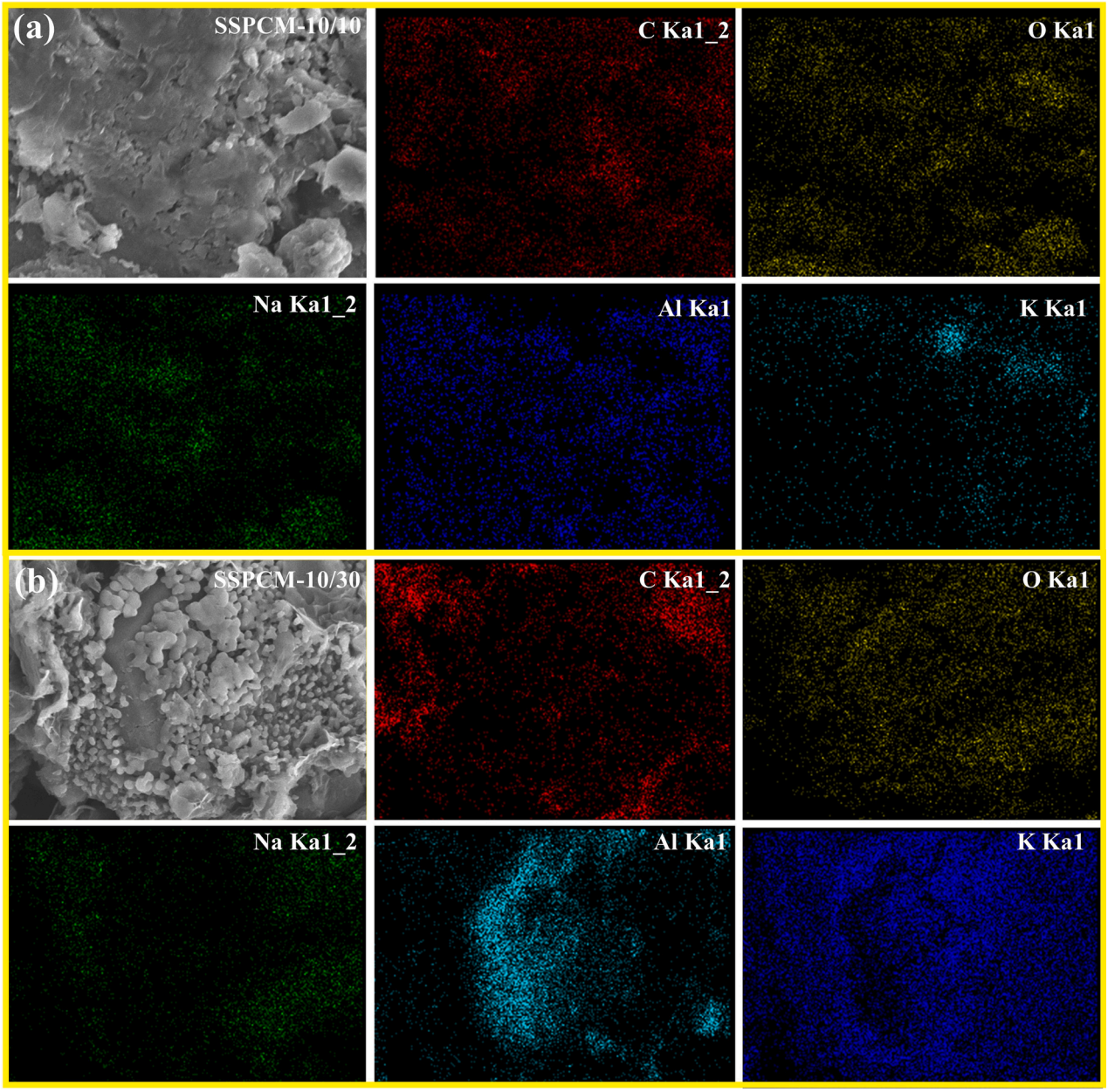

Fig. 7. EDS element mapping images of (a) SSPCM-10/10, (b) SSPCM-10/30 sintered at 300 °C.

larger particles. The surface of SSPCM-10EG had more EG lamellar flakes than SSPCM-5EG, and the SSPCM-10EG had smaller $NaNO_3$-KNO_3 particles that the EG lamellar structure can uniformly adsorb.

3.1.2. *Micro- and macro-morphology of $NaNO_3$-KNO_3/EG/Al_2O_3*

Fig. 4 shows the macroscopic morphology of different SSPCMs at different sintering temperatures. Compared to the composite phase change materials with pure EG adsorption, the morphology of the composites was improved due to the addition of particles as SSMs. Table 3 shows the degree of deformation of the composites. The composites with less mass of SSMs could maintain a better shape at lower sintering temperatures. For example, SSPCM-8/10 and SSPCM-5/20 sintered at 300 °C could be shape-stabilized. However, as the sintering temperature increased, the sample deformation became more severe. For example, SSPCM-8/10 sintered at high temperature, the molten salt leaked because the skeleton support material could not provide enough gap for the volume expansion of the molten salt. Moreover, the molecules are more reactive at higher sintering temperatures due to their higher kinetic energy. This leads to a decrease in the cohesive force of PCM in the liquid state, which in turn leads to a decrease in surface tension [1]. Therefore, if SSPCMs must be applied in a wide temperature range with an upper limit temperature higher than the melting point, more SSMs are needed to support liquid PCMs. SSPCM-8/30 and SSPCM-10/30 sintered at 450 °C could maintain excellent morphology. The maximum mass fraction of $NaNO_3$-KNO_3 was 82.8 wt% for SSPCMs sintered at 300 °C and 66.4 wt% for SSPCMs sintered at 450 °C.

As shown in Fig. 5(a-b), Al_2O_3 showed a spherical structure with a large surface area, and this can provide interfacial forces during the melting of the PCM. The microstructural development of the composites can be explained as follows. $NaNO_3$-KNO_3 was adsorbed in the lamellar structure of EG by the previous impregnation step. A certain pore space between $NaNO_3$-KNO_3/EG and Al_2O_3 was created by mixing and compression. $NaNO_3$-KNO_3 transformed from solid to liquid phase at high sintering temperature and therefore had flow properties. EG could not completely absorb part of $NaNO_3$-KNO_3 due to the pressure difference caused by volume expansion. Then, the liquid entered the Al_2O_3

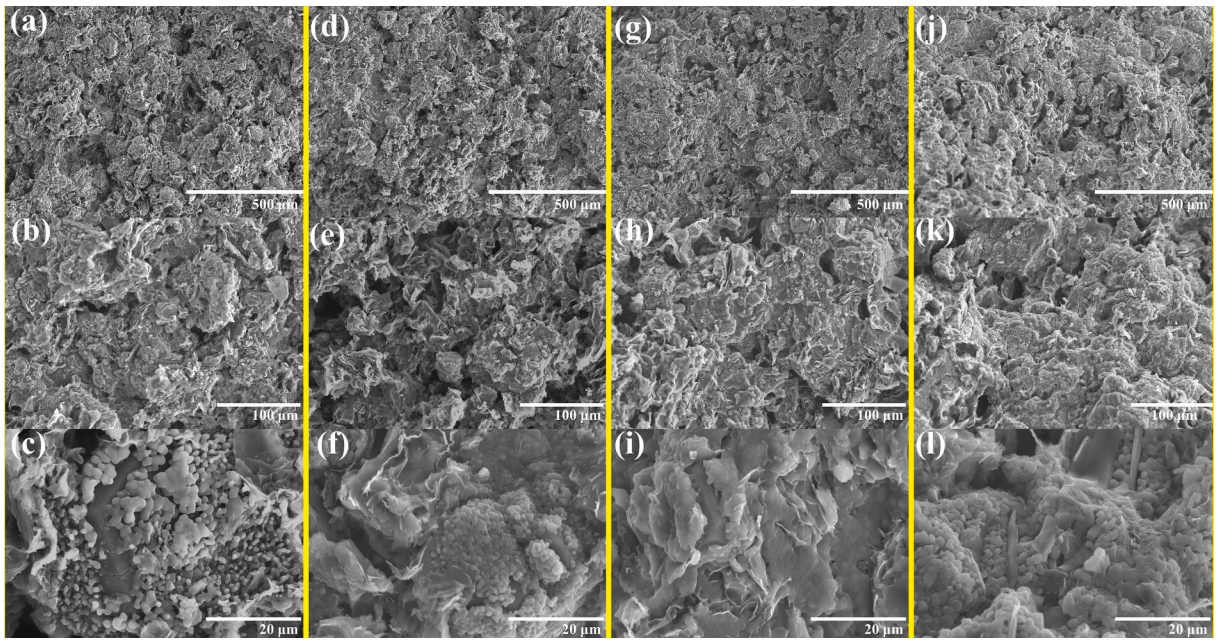

Fig. 8. SEM images of SSPCM-10/30 sintered at (a-c) 300 °C, (d-f) 350 °C, (g-i) 400 °C, and (j-l) 450 °C with the magnification of 100x, 350x, and 2000x.

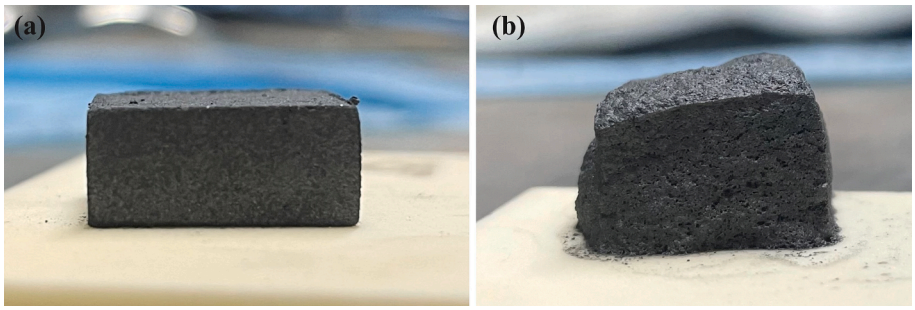

Fig. 9. Macro morphology of SSPCM-8/20 (a) sintered at 350 °C for 2.5 h (b) sintered sample held at 450 °C for 1 h.

gap under pressure. At the same time, the liquid $NaNO_3$-KNO_3 offered the tension to collect the Al_2O_3 particles and bonded them after the salt had solidified. In such a process, a liquid bridge was created between the salt and Al_2O_3 particles to overcome the swelling effect of EG and promote the rigidity and densification of the composite structure [27,26]. Therefore, SSPCMs shaped a dense microstructure after sintering, as shown in the SEM images of the low magnification of the SSPCM in Fig. 6 and Fig. 8. The PCM embedded in the crevices between the lamellar structure of EG and the Al_2O_3 particles prevented the SSPCMs from leaking and deforming during the phase transition [19]. However, if the PCM quantity was too large, the support material could not absorb the entire PCM. Therefore, the PCM would overflow from the support material. Comparing SSPCM-8/30 and SSPCM-10/30 and SSPCM-10/10, SSPCM-10/20 and SSPCM10/30 sintered at 300 °C in Fig. 6, it can be found that the denseness of SSPCM decreases with the decrease of PCM content. PCM in the phase transition process can flow into the voids of Al_2O_3 and $NaNO_3$-KNO_3/EG during the compression process, which makes the material dense after sintering. However, fewer PCMs and more voids between SSMs can lead to poor connections between materials and even more pores.

The positions of EG, Al_2O_3 and $NaNO_3$-KNO_3 of SSPCMs are not easily distinguished by SEM images, but the elemental distribution of each material obtained from the face scan microstructure can distinguish their positions. Fig. 7 shows the elemental distributions of SSPCM-10/10 and SSPCM-10/30 sintered at 300 °C in Fig. 6(f) and Fig. 6(l). In the EDS element mapping, element C represents EG, elements Na and K represent $NaNO_3$-KNO_3, element Al represents Al_2O_3, and element O represents $NaNO_3$-KNO_3 and Al_2O_3. These six elements are evenly distributed in SSPCM, which meant that Al_2O_3, EG and $NaNO_3$-KNO_3 were uniformly distributed in the sintered SSPCM10/10 and SSPCM-10/30. The mass percentage of $NaNO_3$-KNO_3 in SSPCM-10/30 in Fig. 6(j-l) and Fig. 7(b) was relatively smaller, and $NaNO_3$-KNO_3 was granular on the EG and Al_2O_3 surface.

Fig. 8 shows the SEM images with different magnifications of SSPCM-10/30 at different sintering temperatures. Compared to SSPCM-10/30 sintered at 300 °C, SSPCM sintered at higher temperatures at lower magnifications exhibited more pronounced porosity, and PCM sintered at higher temperatures at higher magnifications showed agglomeration on the surface of SSMs. The formation of porosity in SSPCM is due to the inability of SSMs to accommodate the volume change of PCM during melting and the higher liquid–solid thermal expansion coefficient ratio [3]. As the sintering temperature increased, the volume expansion of $NaNO_3$-KNO_3 increased, and the thermal stress acting on the SSMs became larger, causing the denseness/expansion of the SSM particles. During the cooling process, the $NaNO_3$-KNO_3 acting on the SSMs did not return to the voids between the SSMs but adhered more to the SSMs' surface, so some pores were created during the solidification process.

SSPCM-8/20 can keep the shape intact below the sintering temperature of 400 °C(Fig. 4). Fig. 9 (a) shows that SSPCM-8/20 can be shaped after sintering at 350 °C and holding for 2.5 h. However, the

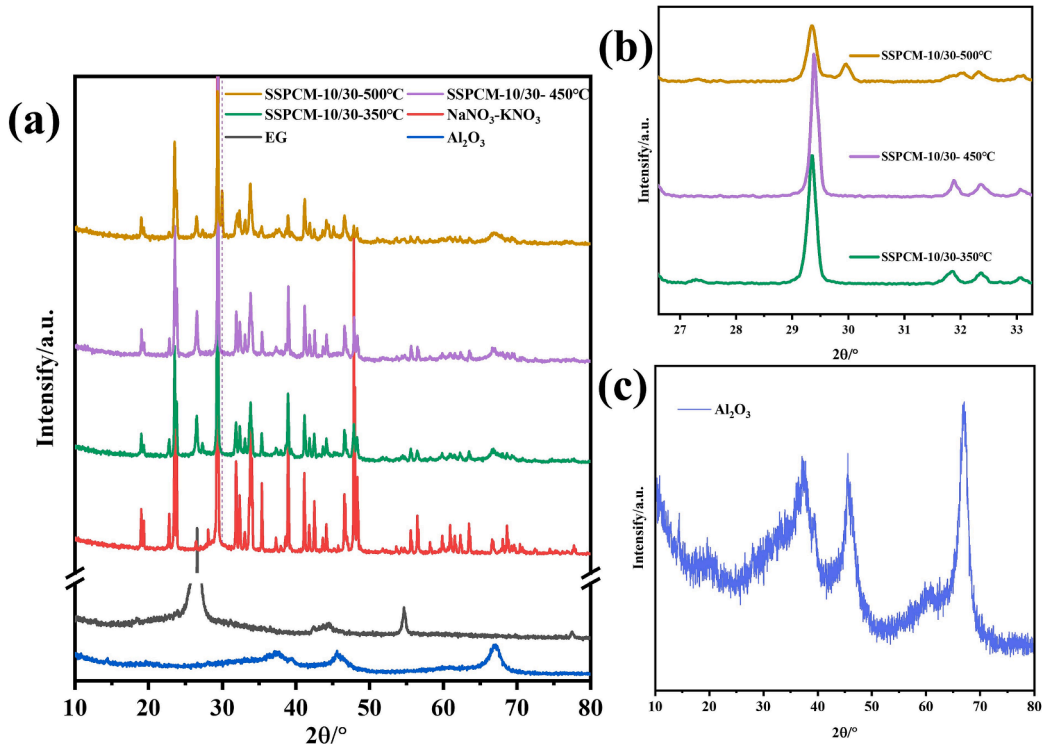

Fig. 10. (a) XRD patterns of the Al_2O_3, EG, $NaNO_3$-KNO_3, SSPCM-10/30 sintered at 350℃, 450℃, 500℃ (b) Enlarged local XRD patterns of the SSPCM-10/30 sintered at 350℃, 450℃, 500℃ (c) XRD pattern of the Al_2O_3.

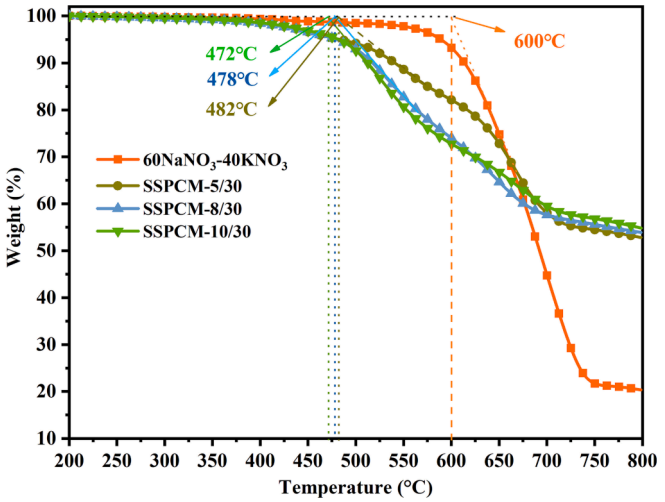

Fig. 11. TG curves of $NaNO_3$-KNO_3, SSPCM-5/30, SSPCM-8/30 and SSPCM-10/30.

deformation of the sample can be observed by holding the sintered sample at 450 °C for 1 h (Fig. 9 (b)). This indicates that samples with lower sintering temperatures may not work at higher temperatures.

3.2. Chemical compatibility analysis of SSPCM-10/30 at different sintering temperatures

Fig. 10(a) shows the XRD patterns of EG, $NaNO_3$-KNO_3, Al_2O_3 and SSPCM-10/30 sintered at 350, 450, and 500 °C. The diffraction peaks of EG and $NaNO_3$-KNO_3 were very sharp, while the reactive Al_2O_3 showed a typical non-crystalline structure, as shown in Fig. 10(c), with no obvious diffraction peaks. The XRD pattern of SSPCM-10/30 sintered at 350 °C and 450 °C contained only peaks of $NaNO_3$-KNO_3 and EG, which indicated that there were no new phases and structures generated. This result demonstrated the excellent chemical stability of EG, $NaNO_3$-KNO_3 and Al_2O_3 when SSPCMs were sintered at 350 °C and 450 °C. However, SSPCM-10/30 sintered at 500 °C showed a significant mass reduction. They were considered to have a diffraction peak of $NaNO_2$ near the peak of 29.5°, as shown in Fig. 10(b), which corresponded to the findings of Lu et al. [35] and Li et al. [31] that the addition of EG decreased the nitrate decomposition temperature. Since EG enhances the polarization of cations on nitrate ions, it makes nitrate more easily decomposed at lower temperatures, as shown in Eq. (1).

$$2NO_3^- = 2NO_2^- + O_2 \quad (1)$$

Further, we analyzed TG for $NaNO_3$-KNO_3, SSPCM-5/30, SSPCM-8/30 and SSPCM-10/30 samples. Fig. 11 shows that the decomposition temperatures of $NaNO_3$-KNO_3, SSPCM-5/30, SSPCM-8/30 and SSPCM-10/30 samples were 600 °C, 482 °C, 478 °C, and 472 °C, where $NaNO_3$-KNO_3 was consistent with the literature [21,7].

3.3. Thermal conductivities of the $NaNO_3$-KNO_3 and SSPCMs at different sintering temperatures

Thermal conductivity is an important parameter affecting the thermal storage and exergy of thermal storage materials. The EG addition can improve the thermal conductivity of the SSPCMs. Fig. 12(a) shows the thermal conductivity of SSPCM-5/30, SSPCM-8/30 and SSPCM-10/30 sintered at 300 °C, 350 °C, 400 °C and 450 °C. Because the shape of SSPCM-5/30 sintered at 450 °C changed severely, we did not measure the corresponding thermal conductivity. The sintering temperature did not significantly affect the thermal conductivity of the same type of samples. The thermal conductivity increased linearly with EG content, as shown in Fig. 12(b). When the EG content was 3.5 wt%, 5.6 wt% and 7 wt%, the average thermal conductivity was 1.10, 1.39 and 1.62 W/(m·K), respectively. These were 2.12, 2.67 and 3.12 times higher than the thermal conductivity of $NaNO_3$-KNO_3(0.52 W/m·K), respectively.

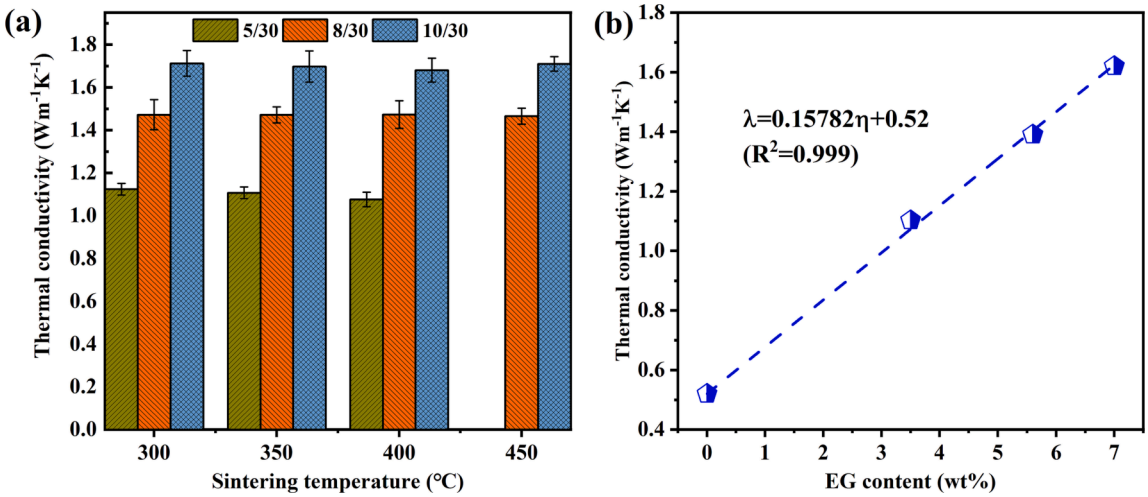

Fig. 12. Thermal conductivity of (a) the SSPCM-5/30, SSPCM-8/30 and SSPCM-10/30 sintered at different temperatures, (b) SSPCMs as a function of EG content.

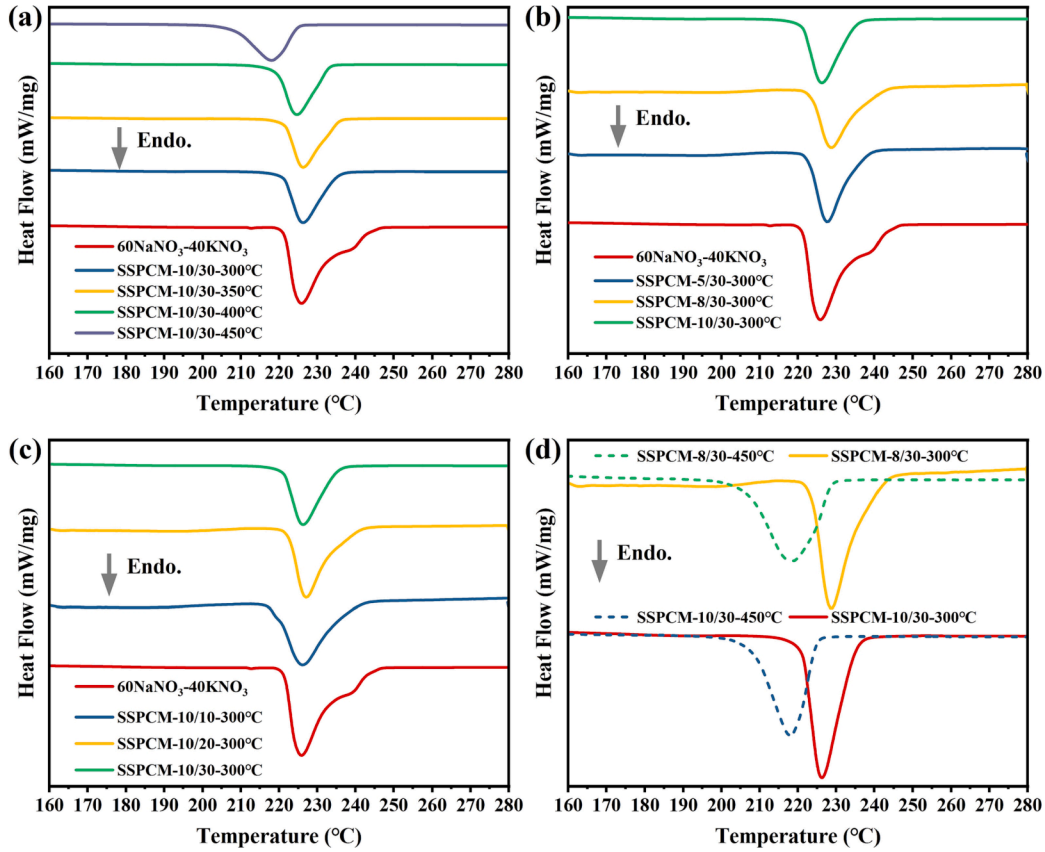

Fig. 13. DSC curves of (a) $NaNO_3$-KNO_3 and SSPCM-10/30 sintered at different temperatures, (b) SSPCMs with different EG contents, (c) SSPCMs with different Al_2O_3 contents, (d) SSPCM-8/30 and SSPCM-10/30 sintered at 300 and 450 °C.

The correlation between the thermal conductivity (λ) and the EG mass fraction (η) of the composite can be approximated by Equation (2):

$$\lambda = 0.15782\eta + 0.52 \ \left(R^2 = 0.999\right) \quad (2)$$

3.4. Phase change behavior of $NaNO_3$-KNO_3 and SSPCMs at different sintering temperatures

Fig. 13(a) compares the thermal properties of $NaNO_3$-KNO_3 and SSPCMs composites at different sintering temperatures. More detailed phase transition parameters are listed in Table 4. The onset and peak temperature of the phase transition of SSPCM-10/30 sintered at 300 °C and 350 °C were almost the same as those of $NaNO_3$-KNO_3, but the onset and the peak temperature of the phase transition of SSPCM-10/30 sintered at 400 °C and 450 °C both showed a certain degree of decrease. In particular, the onset and peak melting temperatures of the samples sintered at 450 °C were significantly lower (Fig. 13(d)). The insertion of EG at higher sintering temperatures leads to the disruption of the molecular forces between $NaNO_3$-KNO_3 and a decrease in surface vapor pressure [50], and thus a decrease in melting point.

Table 4
Phase change properties of the $NaNO_3$-KNO_3 and the SSPCMs sintered at different temperatures.

Sample	T_s (℃)	Onset temperature (℃)	Peak temperature (℃)	Measured latent heat (J/g)	Theoretical latent heat (J/g)
$NaNO_3$-KNO_3	–	221.49	225.82	110.6	110.60
SSPCM-5/30	300	222.89	227.69	61.08	73.55
SSPCM-8/30	300	223.66	228.79	59.22	71.23
SSPCM-8/30	450	206.37	218.65	59.06	71.23
SSPCM-10/10	300	218.84	226.04	82.92	89.59
SSPCM-10/20	300	222.62	227.13	70.90	79.63
SSPCM-10/30	300	221.1	226.29	58.2	69.68
SSPCM-10/30	350	221.43	226.34	57.48	69.68
SSPCM-10/30	400	219.43	224.7	56.51	69.68
SSPCM-10/30	450	207.63	218.06	56.01	69.68

The theoretical latent heat of SSPCMs can be calculated from Equation (3).

$$\Delta H_{theory} = (1 - \eta - \theta)\,\Delta H_{PCM} \quad (3)$$

where ΔH_{theory} is the theoretical latent heat of SSPCM; η and θ are the mass fractions of EG and Al_2O_3; ΔH_{PCM} is the latent heat of $NaNO_3$-KNO_3. The actual measured latent heat of the composite phase change material is lower than the theoretical value., which was consistent with the study of literature [39,53]. The crystal alignment and orientation of the nitrate molecular chains would be limited by steric effects and drag. This may lead to a decrease in the regularity of the grain line region and an increase in lattice defects.

3.5. Compressive strength of $NaNO_3$-KNO_3/EG/Al_2O_3 SSPCMs

The compressive strength decreased with increasing Al_2O_3 content at the same sintering temperature. For example, the compressive strength of SSPCM-10/10 sintered at 300 °C was 62.95 MPa, but SSPCM-10/30 decreased to 38.96 MPa. The macroscopic structures of SSPCMs sintered at 300 °C shown in Fig. 4, SSPCM-8/10 and SSPCM-10/10 could maintain a good shape, which indicated that $NaNO_3$-KNO_3 could bond Al_2O_3 well when it became liquid and the microstructure of SSPCM was dense (as shown in Fig. 6(d-f)). At this sintering temperature, as the Al_2O_3 content increased, the pores between the SSMs increased, and the PCM with less content could not completely cover the pores between the SSMs during the melting process (as shown in Fig. 6(g-l)). The pores that appear inside the SSPCM caused a reduction in compressive strength.

Fig. 14(b) shows the compressive strength of SSPCM-8/10 and SSPCM-10/30 at different sintering temperatures. The compressive strengths of SSPCM-8/10 and SSPCM-10/30 decreased with the sintering temperature increase. As discussed in Section 3.1.2, PCM became liquid from the solid phase and flowed into the void of SSMs at a higher sintering temperature and exerted specific thermal stress on SSMs. As the sintering temperature increased, the PCM in the void of SSMs

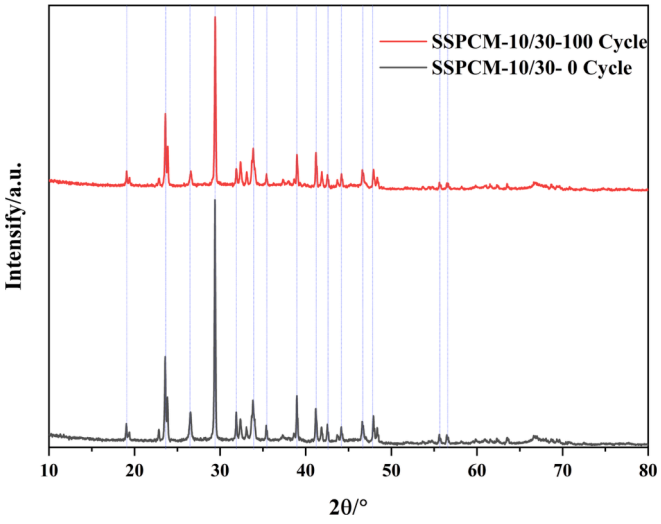

Fig. 15. XRD patterns of SSPCM-10/30 sintered at 450 ℃ before and after 100 thermal cycles.

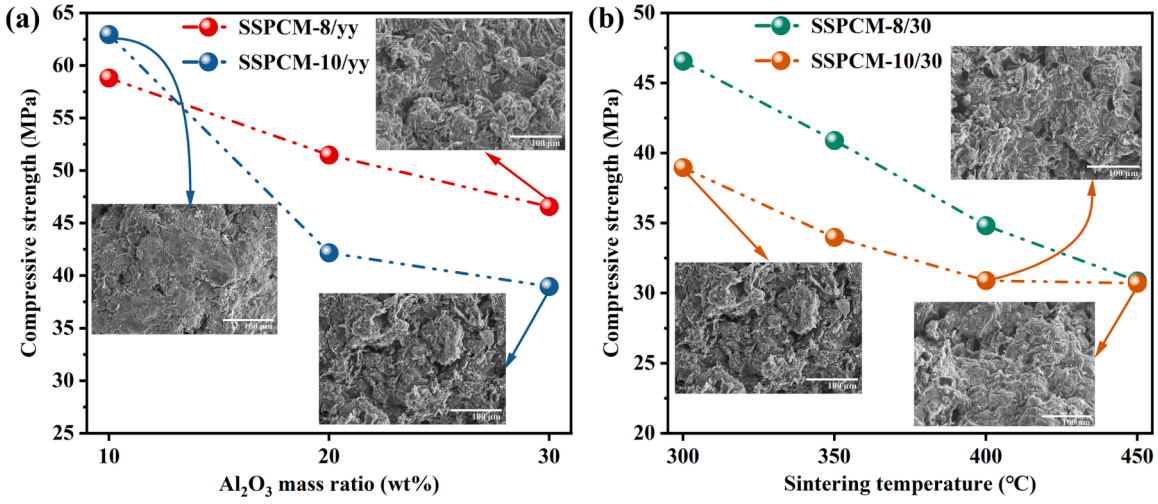

Fig. 14. (a) Effect of Al_2O_3 mass ratio on the compressive strength of SSPCM sintered at 300 °C, (b) Effect of sintering temperature on the compressive strength of SSPCM-8/30 and SSPCM-10/30.

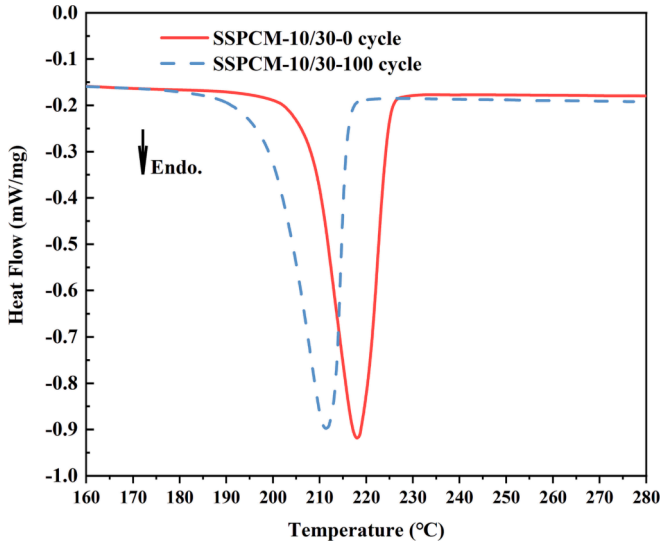

Fig. 16. DSC curves of SSPCM-10/30 sintered at 450 ℃ before and after 100 thermal cycles.

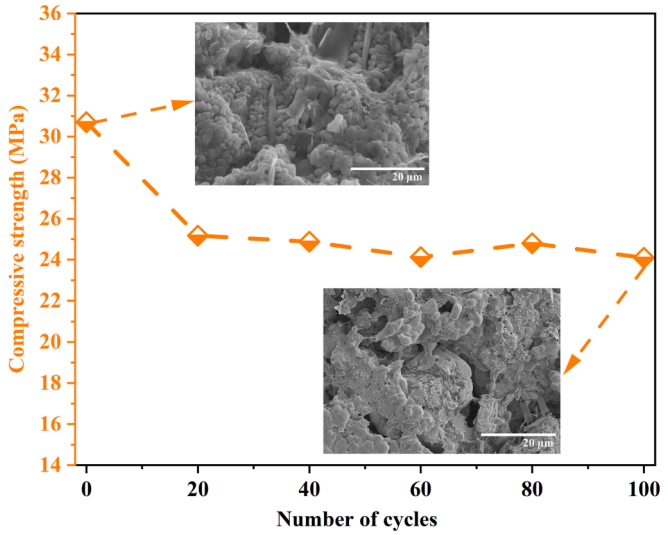

Fig. 17. Compressive strength of SSPCM-10/30 sintered at 450 ℃ before and after 100 thermal cycles.

overpressurized, its thermal stress exerted on SSMs increased, and more PCM adhered to SSMs. PCM did not ultimately flow into the void of SSMs during solidification, so SSPCM presented more and larger pores in the solid phase. Therefore, the compressive strength decreases with the increase in sintering temperature.

3.6. Cycling stability

Fig. 15 shows the XRD patterns of SSPCM-10/30 sintered at 450 °C before and after 100 thermal cycles. The diffraction peaks of the samples before and after cycling corresponded to each other, which indicated the good thermal stability of SSPCM-10/30 without new material generation.

Fig. 16 shows the DSC curves of SSPCM-10/30 sintered at 450 °C before and after 100 thermal cycles. SSPCM-10/30 showed changes in phase transition temperature and latent heat before and after 100 cycles. The onset and peak temperatures of the SSPCM-10/30 changed from 207.63 °C to 199.64 °C and 218.06 °C to 211.37 °C, respectively. From the XRD pattern of Fig. 15, it can be compared that the intensity of $NaNO_3$-KNO_3 after cycling was lower than that of the sample before cycling. This indicates the limitation of the crystallization of $NaNO_3$-KNO_3 in the SSPCM-10/30 after cycling. Usually, the melting temperature of the sample is related to the grain size. If the grain size becomes smaller, the corresponding crystal strength decreases, and the melting point decreases [53,30]. In addition, the higher the crystallinity of PCM, the more regular the arrangement of molecular chains and the higher the melting temperature. The significant volume change of PCM during the cyclic melting of SSPCM-10/30 leads to overpressure. As a result, the matrix undergoes deformation [3] or migration and distribution/redistribution [24]. The matrix plays the role of heterogeneous nucleation in the composite. Changes in the nucleation sites within the material may lead to a decrease in the grain size of $NaNO_3$-KNO_3 and the melting temperature. The latent heat of SSPCM-10/30 decreased from 56.01 J/g to 53.44 J/g, a decrease of 2.57 J/g. This may be due to the evaporation and leakage of $NaNO_3$-KNO_3 during repeated thermal cycling of SSPCMs [39,47].

Fig. 17 shows the compressive strength curves of SSPCM-10/30 sintered at 450 °C before and after 100 heating and cooling cycles. The compressive strength of SSPCM-10/30 was 30.7 MPa before cycling and became 25.17 MPa after 20 cycles. The compressive strength decreased by 18%. This may be because the samples before cycling were cooled slowly under the cooling procedure of 5 °C/min, while the SSPCMs for cycling tests were cooled at room temperature. The compressive strength decreased due to the sudden cooling of SSPCMs and the samples' drastic degree of cold shrinkage. By comparing the SEM images of SSPCM-10/30 sintered at 450 °C before and after 100 cycles in Fig. 5 and Fig. 18, larger gaps can be seen in the post-cycle samples, which may explain the decrease in compressive strength. The compressive strength did not change much after 20 cycles, which means that the compressive strength reached equilibrium after 20 cycles.

3.7. Performance comparison

Table 5 compares the properties of other SSPCMs containing inorganic salts prepared by the CCHS method with the SSPCMs fabricated in the present work ($NaNO_3$-KNO_3/Al_2O_3/EG). It can be seen that the use of ceramic-based materials can lead to better compressive strength of SSPCMs. However, excessive sintering temperatures reduce the compressive strength considering the thermal expansion effect of inorganic salts. For example, $\Delta T_{s\text{-}m}$ is about 332 °C, and the compressive strength is ≤28 MPa in the literature [40]. Therefore, it is necessary to consider the effect of sintering temperature on compressive strength according to the discussion in Section 3.2 of this paper. Adding too much EG will result in a significantly increased thermal conductivity, but the material's compressive strength will be reduced. The addition of TCEAs to SSPCMs can increase the thermal conductivity of the material. The thermal conductivity of the SSPCMs prepared in this paper is less than that of the EG-based SSPCMs prepared by Ren et al. [39]. However, the growth pattern of thermal conductivity after the addition of EG to the material is similar to the literature [44,45], which indicates the experiment's reliability. The reason may be that the EG thermal conductivity is in the range of 4–100 W/(m·K) [14] and the difference in the operating pressure of SSPCMs [14], so the material properties are different. Overall, the present material's thermal conductivity and compressive strength properties are more excellent after the addition of EG.

4. Conclusion

The present work aims to promote the application of SSPCMs based on $NaNO_3$-KNO_3 as PCM in a wide temperature window. We proposed SSPCMs with $NaNO_3$-KNO_3 as PCM, Al_2O_3 as SSM, and EG as TCEA and SSM. Solution impregnation to fabricate $NaNO_3$-KNO_3/EG and cold pressing and sintering were used to manufacture SSPCMs. SSPCMs prepared with different sintering temperatures were investigated for their chemical stability, macro- and micro-morphology, thermal

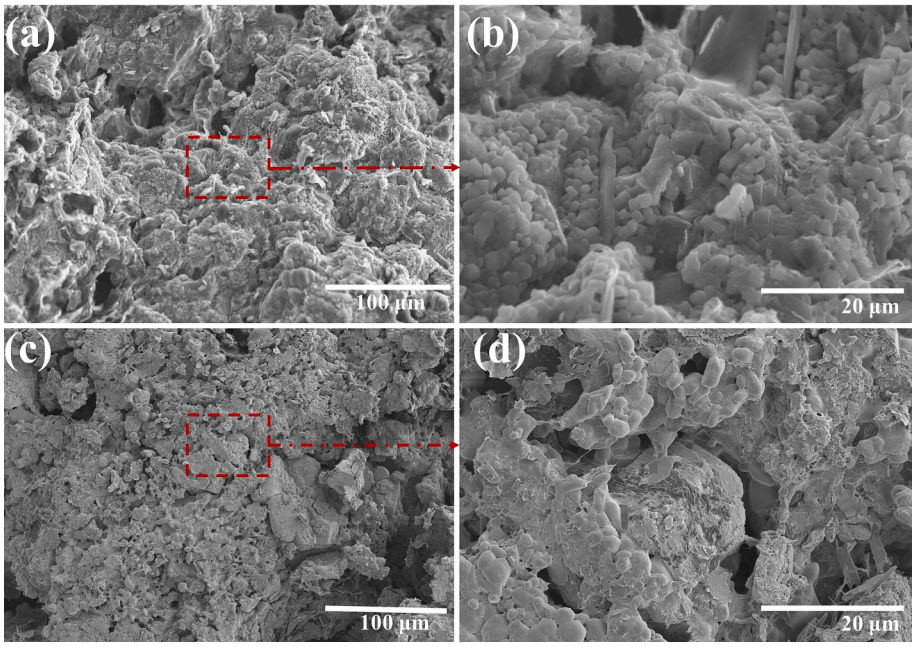

Fig. 18. SEM image of SSPCM-10/30 sintered at 450 ℃ (a-b) before and (c-d) after 100 cycles.

Table 5
Performance comparison of SSPCMs prepared in this paper with SSPCMs containing other inorganic salts prepared by CCHS.

PCM	SSMs	PCM (wt%)	ΔH_{PCM} (J/g)	ΔH_{SSPCMs} (J/g)	$T_{m\text{-}PCM}$(℃)	Ts (℃)	Φ (mm)	Pressure (MPa)	Compressive strength (MPa)	λ (W/(m·K))	Ref.
$NaNO_3$	Carbide slag	52.5	171.13	65.97	302.7	340℃ for 2 h	13	10	54.5	–	[51]
		50		59.61					73.6	0.93 (350℃)	
		40		41.91					59.5	–	
$NaNO_3$	Sludge-incinerated ash	55	139.3	77.21	303.9	340℃ for 1.5 h	13	72	115.47	–	[47]
		50		60.33					139.65	0.955 (100℃)	
		45		57.45					61.10	–	
K_2CO_3-Li_2CO_3-Na_2CO_3 (1:2:1)[a]	MgO	60	327.6	183.1	399.6	600℃ for 1.5 h	12.5	70	20	–	[40]
		50		158.7					28	–	
		40		125.5					25	–	
50KCl-50LiCl	19EG:5SiC	76	223	168.2	355.7	500 °C for 1 h	12.5	25	~6	–	[41]
	18EG:10SiC	72		161.5					~9	–	
	17EG:15SiC	68		153.2					~8.7	–	
	16EG:20SiC	64		146.7					~6	–	
	15EG:25SiC	60		141.2					~5.7	–	
60$NaNO_3$-40KNO_3	Red mud	60	110.4	58.14	223.85	Heated to 400 ℃ for 5℃/min	13	100	–	~0.83	[2]
		50		48.29					–	~0.70	
		40		35.99					–	~0.71	
60$NaNO_3$-40KNO_3	Red mud + 5 wt % Graphite	48.5	110.4	46.25	223.85	Heated to 400 ℃ for 5℃/min	13	100	–	~0.78	[3]
		57.5		51.92					–	~0.8	
$Ca(NO_3)_2$-KNO_3-$NaNO_3$-$NaNO_2$	MgO	50	72.53	39.89	96.7	250℃ for 1 h	12.5	50	–	0.954	[27]
	MgO + 10% graphite	45		37.71					–	1.41	
$Ca(NO_3)_2$-$NaNO_3$(3:7)[a]	EG	95	130	98.01	221.7	300 °C for 3 h	13	8	–	~2.4	[39]
		94		94.3					–	~4.8	
		93		89.79					–	~5.6	
60$NaNO_3$-40KNO_3	Al_2O_3 + EG	81	110.6	89.59	225.8	300	15 × 15	16	62.95	–	This work
		63		58.2		300			38.96	1.62	
		63		57.48		350			33.98		
		63		56.01		450			30.7		

[a] Represents the mole ratio.

conductivity, mechanical properties, thermal properties, and cyclic stability performance at different sintering temperatures. The main conclusions drawn are as follows.

(1) The mass fraction of PCM determines the latent heat of SSPCMs. The maximum $NaNO_3$-KNO_3 mass fraction in SSPCMs decreased with the increasing sintering temperature. The maximum mass fraction of $NaNO_3$-KNO_3 was 82.8 wt% for SSPCMs sintered at 300 °C and 66.4 wt% for SSPCMs sintered at 450 °C. Samples with application temperatures higher than the sintering temperature may have problems stabilizing the shape.

(2)EG, Al_2O_3 and nitrate do not react chemically, but the addition of EG decreases the decomposition temperature of the composite.

(3) The thermal conductivity of SSPCMs increases nearly linearly with the EG mass fraction. When the EG mass fraction was 7 wt%, the average thermal conductivity was 1.62 W/(m·K), 3.12 times higher than $NaNO_3$-KNO_3. The sintering temperature had no significant effect on the thermal conductivity of the same type of SSPCMs.

(4)The latent heat of SSPCM-10/30 decreases slightly at different sintering temperatures. The starting melting temperatures of SSPCMs-10/30 sintered at 300 °C and 350 °C were consistent with that of pure $NaNO_3$-KNO_3. However, SSPCMs-10/30 sintered at 400 °C and 450 °C started melting from 219.43 °C and 207.43 °C, respectively, which were lower than that of pure $NaNO_3$-KNO_3. SSPCMs-8/30 corroborated this point.

(5) The compressive strength of SSPCMs sintered at 300 °C decreased with increasing the mass fraction of Al_2O_3. Moreover, the compressive strength of the same SSPCMs decreased with increasing sintering temperature. Among them, SSPCM-10/10 reached a maximum compressive strength of 62.95 MPa when sintered at 300 °C, and SSPCM-10/30 reached a minimum compressive strength of 30.7 MPa when sintered at 450 °C.

(6) XRD results showed that SSPCM-10/30 sintered at 450 °C had good thermal stability after 100 cycles. The latent heat decreased from 56.01 J/g to 53.44 J/g. The compressive strength dropped from 30.7 MPa to 25.17 MPa before and after 20 cycles due to larger internal gaps and did not change much after 20 cycles.

Declaration of Competing Interest

The authors declare that they have no known competing financial interests or personal relationships that could have appeared to influence the work reported in this paper.

Acknowledgement

This work was Supported by the Fundamental Research Funds for the Central Universities (2022ZFJH004).

References

[1] Anagnostopoulos, A., Navarro, H., Alexiadis, A., Ding, Y., 2020. Wettability of NaNO3 and KNO3 on MgO and carbon surfaces-understanding the substrate and the length scale effects. J. Phys. Chem. C 124, 8140–8152. https://doi.org/10.1021/acs.jpcc.0c00978.

[2] Anagnostopoulos, A., Navarro, M.E., Stefanidou, M., Ding, Y., Gaidajis, G., 2021. Red mud-molten salt composites for medium-high temperature thermal energy storage and waste heat recovery applications. J. Hazard. Mater. 413 https://doi.org/10.1016/j.jhazmat.2021.125407.

[3] Anagnostopoulos, A., Navarro, M.E., Stefanidou, M., Seferlis, P., Gaidajis, G., Ding, Y., 2021. Effect of carbon on the performance of red mud-molten salt composites for thermal management and waste heat recovery applications. J. Energy Storage 44, 103363. https://doi.org/10.1016/j.est.2021.103363.

[4] Bradshaw, R.W., 2009. Effect of composition on the density of multi-component molten nitrate salts. Mater. Chem. https://doi.org/10.2172/983681.

[5] Busca, G., 2014. The surface of transitional aluminas: a critical review. Catal. Today 226, 2–13. https://doi.org/10.1016/j.cattod.2013.08.003.

[6] Deng, Y., Li, J., Qian, T., Guan, W., Wang, X., 2017. Preparation and characterization of KNO3/diatomite shape-stabilized composite phase change material for high temperature thermal energy storage. J. Mater. Sci. Technol. 33, 198–203. https://doi.org/10.1016/j.jmst.2016.02.011.

[7] Dunn, R.I., Hearps, P.J., Wright, M.N., 2012. Molten-salt power towers: Newly commercial concentrating solar storage. Proc. IEEE 100, 504–515. https://doi.org/10.1109/JPROC.2011.2163739.

[8] Ge, Z., Ye, F., Cao, H., Leng, G., Qin, Y., Ding, Y., 2014. Carbonate-salt-based composite materials for medium- and high-temperature thermal energy storage. Particuology 15, 77–81. https://doi.org/10.1016/j.partic.2013.09.002.

[9] Gielen, D., Boshell, F., Saygin, D., Bazilian, M.D., Wagner, N., Gorini, R., 2019. The role of renewable energy in the global energy transformation. Energy Strateg. Rev. 24, 38–50. https://doi.org/10.1016/j.esr.2019.01.006.

[10] Griffin, P.W., Hammond, G.P., 2019. Industrial energy use and carbon emissions reduction in the iron and steel sector: a UK perspective. Appl. Energy 249, 109–125. https://doi.org/10.1016/j.apenergy.2019.04.148.

[11] Guo, Q., Wang, T., 2015. Study on preparation and thermal properties of sodium nitrate/silica composite as shape-stabilized phase change material. Thermochim. Acta 613, 66–70. https://doi.org/10.1016/j.tca.2015.05.023.

[12] Hou, Y., Qiu, J., Wang, W., He, X., Ayyub, M., Shuai, Y., 2022. Preparation and performance improvement of chlorides/MgO ceramics shape-stabilized phase change materials with expanded graphite for thermal energy storage system. Appl. Energy 316. https://doi.org/10.1016/j.apenergy.2022.119116.

[13] Ibrahim, A., Peng, H., Riaz, A., Abdul Basit, M., Rashid, U., Basit, A., 2021. Molten salts in the light of corrosion mitigation strategies and embedded with nanoparticles to enhance the thermophysical properties for CSP plants. Sol. Energy Mater. Sol. Cells 219, 110768. https://doi.org/10.1016/j.solmat.2020.110768.

[14] Jiang, F., Zhang, L., She, X., Li, C., Cang, D., Liu, X., Xuan, Y., Ding, Y., 2020. Skeleton materials for shape-stabilization of high temperature salts based phase change materials: a critical review. Renew. Sustain. Energy Rev. 119 https://doi.org/10.1016/j.rser.2019.109539.

[15] Jiang, Y., Liu, M., Sun, Y., 2019. Review on the development of high temperature phase change material composites for solar thermal energy storage. Sol. Energy Mater. Sol. Cells 203. https://doi.org/10.1016/j.solmat.2019.110164.

[16] Jiang, Y., Sun, Y., Jacob, R.D., Bruno, F., Li, S., 2018. Novel Na2SO4-NaCl-ceramic composites as high temperature phase change materials for solar thermal power plants (Part I). Sol. Energy Mater. Sol. Cells 178, 74–83. https://doi.org/10.1016/j.solmat.2017.12.034.

[17] Jiang, Y., Sun, Y., Li, S., 2019. Performance of novel Na 2 SO 4 -NaCl-ceramic composites as high temperature phase change materials for solar power plants (Part II). Sol. Energy Mater. Sol. Cells 194, 285–294. https://doi.org/10.1016/j.solmat.2018.05.028.

[18] Jiang, Z., Jiang, F., Li, C., Leng, G., Zhao, X., Li, Y., Zhang, T., Xu, G., Jin, Y., Yang, C., Ding, Y., 2019. A form stable composite phase change material for thermal energy storage applications over 700 °C. Appl. Sci. 9 https://doi.org/10.3390/app9050814.

[19] Jiang, Z., Leng, G., Ye, F., Ge, Z., Liu, C., Wang, L., Huang, Y., Ding, Y., 2015. Form-stable LiNO3-NaNO3-KNO3-Ca(NO3)2/calcium silicate composite phase change material (PCM) for mid-low temperature thermal energy storage. Energy Convers. Manag. 106, 165–172. https://doi.org/10.1016/j.enconman.2015.09.035.

[20] Jiang, Z., Palacios, A., Zou, B., Zhao, Y., Deng, W., Zhang, X., Ding, Y., 2022. A review on the fabrication methods for structurally stabilised composite phase change materials and their impacts on the properties of materials. Renew. Sustain. Energy Rev. 159 https://doi.org/10.1016/j.rser.2022.112134.

[21] Kearney, D., Herrmann, U., Nava, P., Kelly, B., Mahoney, R., Pacheco, J., Cable, R., Potrovitza, N., Blake, D., Price, H., 2003. Assessment of a molten salt heat transfer fluid in a parabolic trough solar field. J. Sol. Energy Eng. Trans. ASME 125, 170–176. https://doi.org/10.1115/1.1565087.

[22] Kenisarin, M.M., 2010. High-temperature phase change materials for thermal energy storage. Renew. Sustain. Energy Rev. 14, 955–970. https://doi.org/10.1016/j.rser.2009.11.011.

[23] Leng, G., Qiao, G., Jiang, Z., Xu, G., Qin, Y., Chang, C., Ding, Y., 2018. Micro encapsulated & form-stable phase change materials for high temperature thermal energy storage. Appl. Energy 217, 212–220. https://doi.org/10.1016/j.apenergy.2018.02.064.

[24] Li, C., Li, Q., Cong, L., Li, Y., Liu, X., Xuan, Y., Ding, Y., 2019. Carbonate salt based composite phase change materials for medium and high temperature thermal energy storage: A microstructural study. Sol. Energy Mater. Sol. Cells 196, 25–35. https://doi.org/10.1016/j.solmat.2019.03.035.

[25] Li, C., Li, Q., Lu, X., Ge, R., Du, Y., Xiong, Y., 2022. Inorganic salt based shape-stabilized composite phase change materials for medium and high temperature thermal energy storage: ingredients selection, fabrication, microstructural characteristics and development, and applications. J. Energy Storage 55. https://doi.org/10.1016/j.est.2022.105252.

[26] Li, Q., Cong, L., Zhang, X., Dong, B., Zou, B., Du, Z., Xiong, Y., Li, C., 2020. Fabrication and thermal properties investigation of aluminium based composite phase change material for medium and high temperature thermal energy storage. Sol. Energy Mater. Sol. Cells 211. https://doi.org/10.1016/j.solmat.2020.110511.

[27] Li, Q., Wei, W., Li, Y., Li, C., Ge, R., Du, Y., Zhang, X., Wu, Y., 2022. Development and investigation of form-stable quaternary nitrate salt based composite phase change material with extremely low melting temperature and large temperature range for low-mid thermal energy storage. Energy Reports 8, 1528–1537. https://doi.org/10.1016/j.egyr.2021.12.054.

[28] Li, R., Zhu, J., Zhou, W., Cheng, X., Li, Y., 2016. Thermal properties of sodium nitrate-expanded vermiculite form-stable composite phase change materials. Mater. Des. 104, 190–196. https://doi.org/10.1016/j.matdes.2016.05.039.

[29] Li, R., Zhu, J., Zhou, W., Cheng, X., Li, Y., 2016. Thermal compatibility of Sodium Nitrate/Expanded Perlite composite phase change materials. Appl. Therm. Eng. 103, 452–458. https://doi.org/10.1016/j.applthermaleng.2016.03.108.

[30] Li, Y., Jiang, S.L., Wang, C.G., Zhu, Q.Z., 2022. Effect of EG particle size on the thermal properties of NaNO3–NaCl/EG shaped composite phase change materials. Energy 239. https://doi.org/10.1016/j.energy.2021.122062.

[31] Li, Y., Yue, G., Yu, Y.M., Zhu, Q.Z., 2020. Preparation and thermal characterization of LiNO3–NaNO3–KCl ternary mixture and LiNO3–NaNO3–KCl/EG composites. Energy 196. https://doi.org/10.1016/j.energy.2020.117067.

[32] Liu, F., Tait, S., Schellart, A., Mayfield, M., Boxall, J., 2020. Reducing carbon emissions by integrating urban water systems and renewable energy sources at a community scale. Renew. Sustain. Energy Rev. 123 https://doi.org/10.1016/j.rser.2020.109767.

[33] Liu, J., Wang, Q., Ling, Z., Fang, X., Zhang, Z., 2017. A novel process for preparing molten salt/expanded graphite composite phase change blocks with good uniformity and small volume expansion. Sol. Energy Mater. Sol. Cells 169, 280–286. https://doi.org/10.1016/j.solmat.2017.05.046.

[34] Liu, L., Wang, L., Ge, W., Ge, Y., Huang, Y., 2019. Effect of particle size on the thermal performance of NaNO3/SiO2/C composite phase-change materials. Particuology 44, 169–175. https://doi.org/10.1016/j.partic.2018.03.012.
[35] Lu, W., Liu, G., Xiong, Z., Wu, Z., Zhang, G., 2020. An experimental investigation of composite phase change materials of ternary nitrate and expanded graphite for medium-temperature thermal energy storage. Sol. Energy 195, 573–580. https://doi.org/10.1016/j.solener.2019.11.102.
[36] Miliozzi, A., Chieruzzi, M., Torre, L., 2019. Experimental investigation of a cementitious heat storage medium incorporating a solar salt/diatomite composite phase change material. Appl. Energy 250, 1023–1035. https://doi.org/10.1016/j.apenergy.2019.05.090.
[37] Qin, Y., Yu, X., Leng, G.H., Zhang, L., Ding, Y.L., 2014. Effect of diatomite content on diatomite matrix based composite phase change thermal storage material. Mater. Res. Innov. 18, S2453–S2456. https://doi.org/10.1179/1432891714Z.000000000449.
[38] Ren, Y., Xu, C., Wang, T., Tian, Z., Liao, Z., 2020. A study of manufacturing processes of composite form-stable phase change materials based on Ca(No3)2–NaNo3 and expanded graphite. Materials (Basel) 13, 1–15. https://doi.org/10.3390/ma13235368.
[39] Ren, Y., Xu, C., Yuan, M., Ye, F., Ju, X., Du, X., 2018. Ca(NO3)2-NaNO3/expanded graphite composite as a novel shape-stable phase change material for mid- to high-temperature thermal energy storage. Energy Convers. Manag. 163, 50–58. https://doi.org/10.1016/j.enconman.2018.02.057.
[40] Sang, L., Li, F., Xu, Y., 2019. Form-stable ternary carbonates/MgO composite material for high temperature thermal energy storage. Sol. Energy 180, 1–7. https://doi.org/10.1016/j.solener.2019.01.002.
[41] Sang, L., Xu, Y., 2020. Form stable binary chlorides/expanded graphite composite material with enhanced compressive strength for high temperature thermal storage. J. Energy Storage 31. https://doi.org/10.1016/j.est.2020.101611.
[42] Sari, A., Karaipekli, A., Alkan, C., 2009. Preparation, characterization and thermal properties of lauric acid/expanded perlite as novel form-stable composite phase change material. Chem. Eng. J. 155, 899–904. https://doi.org/10.1016/j.cej.2009.09.005.
[43] Suleiman, B., Yu, Q., Ding, Y., Li, Y., 2019. Fabrication of form stable NaCl-Al2O3 composite for thermal energy storage by cold sintering process. Front. Chem. Sci. Eng. 13, 727–735. https://doi.org/10.1007/s11705-019-1823-2.
[44] Tian, H., Wang, W., Ding, J., Wei, X., Huang, C., 2016. Preparation of binary eutectic chloride/expanded graphite as high-temperature thermal energy storage materials. Sol. Energy Mater. Sol. Cells 149, 187–194. https://doi.org/10.1016/j.solmat.2015.12.038.
[45] Wang, T., Wang, K., Ye, F., Ren, Y., Xu, C., 2021. Characterization and thermal properties of a shape-stable Na2CO3-K2CO3/coal fly ash/expanded graphite composite phase change materials for high-temperature thermal energy storage. J. Energy Storage 33, 102123. https://doi.org/10.1016/j.est.2020.102123.
[46] Wang, W., Yang, X., Fang, Y., Ding, J., 2009. Preparation and performance of form-stable polyethylene glycol/silicon dioxide composites as solid-liquid phase change materials. Appl. Energy 86, 170–174. https://doi.org/10.1016/j.apenergy.2007.12.003.
[47] Xiong, Y., Song, C., Ren, J., Jin, Y., Nie, B., Xu, Q., Wu, Y., Li, C., Li, H., Ding, Y., 2022. Sludge-incinerated ash based shape-stable phase change composites for heavy metal fixation and building thermal energy storage. Process Saf. Environ. Prot. 162, 346–356. https://doi.org/10.1016/j.psep.2022.04.004.
[48] Xu, B., Ma, H., Lu, Z., Li, Z., 2015. Paraffin/expanded vermiculite composite phase change material as aggregate for developing lightweight thermal energy storage cement-based composites. Appl. Energy 160, 358–367. https://doi.org/10.1016/j.apenergy.2015.09.069.
[49] Xu, G., Leng, G., Yang, C., Qin, Y., Wu, Y., Chen, H., Cong, L., Ding, Y., 2017. Sodium nitrate – diatomite composite materials for thermal energy storage. Sol. Energy 146, 494–502. https://doi.org/10.1016/j.solener.2017.03.003.
[50] Xu, T., Li, Y., Chen, J., Liu, J., 2017. Preparation and thermal energy storage properties of LiNO3-KCl-NaNO3/expanded graphite composite phase change material. Sol. Energy Mater. Sol. Cells 169, 215–221. https://doi.org/10.1016/j.solmat.2017.05.035.
[51] Yaxuan, X., Huixiang, W., Yuting, W., Jinhua, Z., Haimeng, L., Qian, X., Xingxing, Z., Chuan, L., Yulong, D., 2022. Carbide slag based shape-stable phase change materials for waste recycling and thermal energy storage. J. Energy Storage 50. https://doi.org/10.1016/j.est.2022.104256.
[52] Ye, F., Ge, Z., Ding, Y., Yang, J., 2014. Multi-walled carbon nanotubes added to Na2CO3/MgO composites for thermal energy storage. Particuology 15, 56–60. https://doi.org/10.1016/j.partic.2013.05.001.
[53] Yu, Q., Lu, Y., Zhang, C., Zhang, X., Wu, Y., Sciacovelli, A., 2020. Preparation and thermal properties of novel eutectic salt/nano-SiO2/ expanded graphite composite for thermal energy storage. Sol. Energy Mater. Sol. Cells 215. https://doi.org/10.1016/j.solmat.2020.110590.
[54] Yuan, F., Li, M.J., Ma, Z., Jin, B., Liu, Z., 2018. Experimental study on thermal performance of high-temperature molten salt cascaded latent heat thermal energy storage system. Int. J. Heat Mass Transf. 118, 997–1011. https://doi.org/10.1016/j.ijheatmasstransfer.2017.11.024.
[55] Zhang, T., Wang, T., Wang, K., Xu, C., Ye, F., 2021. Development and characterization of NaCl-KCl/Kaolin composites for thermal energy storage. Sol. Energy 227, 468–476. https://doi.org/10.1016/j.solener.2021.09.020.